



A pseudo three-dimensional electrochemical–thermal model of a prismatic LiFePO₄ battery during discharge process



Meng Xu ^{a, b}, Zhuqian Zhang ^{a, b, *}, Xia Wang ^c, Li Jia ^{a, b}, Lixin Yang ^{a, b}

^a Institute of Thermal Engineering, School of Mechanical, Electronic and Control Engineering, Beijing Jiaotong University, China

^b Beijing Key Laboratory of Flow and Heat Transfer of Phase Changing in Micro and Small Scale, China

^c Department of Mechanical Engineering, Oakland University, Rochester, MI 48309, USA

ARTICLE INFO

Article history:

Received 22 December 2013

Received in revised form

20 November 2014

Accepted 27 November 2014

Available online 23 December 2014

Keywords:

Lithium ion battery

Cell unit

Electrochemical–thermal coupled model

Current collecting tabs

Three-dimension

Lithium iron phosphate

ABSTRACT

A lithium ion battery consists of numerous electrochemical cell units. Thermal and electrical behaviors of these local cell units have great influence on the battery's performance and safety. To study the relationship between the cell units and the battery cell, a pseudo 3D (three-dimensional) model was developed for a prismatic LiFePO₄ battery by coupling the mass, charge, and energy conservations, as well as the cell electrochemical kinetics. The model treated the battery with current collecting tabs as 3D and the local cell units as 1D. Both electrochemical and thermal characteristics of the battery were studied by using this simplified model during the discharge process. A uniformity index characterizing the SOC (state of charge) distributions among 1D cell units was also introduced. This index was used to investigate the effects of the tab placement on the uniformity of the battery cell. The placement of the positive and negative current collecting tabs on the prismatic battery was found to have a significant effect on the distributions of its potential and local reaction rates, which therefore affect the heat generation rate, and thus the temperature distribution within the battery.

© 2014 Elsevier Ltd. All rights reserved.

1. Introduction

LiFePO₄ (Lithium ion phosphate) batteries are becoming preferred energy storage devices for electric vehicles. Compared to other lithium electrochemistries, the LiFePO₄ batteries have the following benefits: more stable and higher DVP (discharge voltage platform), larger capacity with reduced weight, low cost, and nontoxicity [1,2]. However, the issues of the high heat generation rate and the non-uniformity of the current density distribution are significant challenges faced by automakers [3–5]. The performance of a high capacity lithium ion battery is influenced by its geometrical characteristics, the placement of the current collecting tabs, and operating conditions. Larger sizes and extreme operating conditions could lead to pronounced non-uniform thermal and electrical behaviors [6]. Therefore large capacity lithium ion batteries require a more comprehensive understanding of their electrochemical fundamentals and thermal behavior.

Modeling and simulation of lithium ion batteries are becoming increasingly important in developing a fundamental understanding of electrochemical performances and thermal characteristics to improve battery thermal management systems [7]. In recent published work, several mathematical models, such as equivalent circuit models [8,9], single particle models [10,11], 1D electrochemical–thermal coupled cell unit models [12–16], and 3D lumped thermal models [17–19], have been developed to predict the electrochemical process, charging and discharging behaviors, and heat generation within the lithium ion battery. The equivalent circuit model [8,9], which is comprised of resistors and the voltage source, is commonly used in electrochemical impedance characterization of lithium-ion battery. The single particle model [10,11] is a simplified model by ignoring the concentration gradient of the electrolyte. The three dimensional lumped thermal model treats the layer structure of the cell unit as homogeneous material with uniform thermal properties, temperature distribution, and heat generation [17–19]. Most of these three dimensional lumped thermal models, however, do not consider the electrochemical reactions. Instead, the heat generation due to the electrochemical reaction is simply added to the energy equation as a source term. One-dimensional cell unit models, on the other hand, comprise

* Corresponding author. Institute of Thermal Engineering, School of Mechanical Electronic and Control Engineering, Beijing Jiaotong University, Beijing 100044, China. Tel.: +86 10 51684329.

E-mail address: zhqzhang@bjtu.edu.cn (Z. Zhang).

conservation of mass, charge, energy, and electrochemical reaction. One-dimensional cell unit models were developed based on the kinetics models to solve the electrochemical and/or thermal characteristics of the cell unit [12–16]. Nevertheless, the one-dimensional cell unit model was developed only for the core structure-cell unit of the battery and thus is incapable of investigating the electrochemical and thermal characteristics of the whole battery cell, or the influence of the current collecting tabs present in commercially available batteries. In addition, most of the studies of the Li-ion battery behavior were based on the LiMnO_4 [20–22], and LiCoO_2 [17,18] chemistries. For batteries with LiFePO_4 (LFP) electrodes, only a handful of kinetic modeling studies have been published [23–25], despite these batteries' many advantages over the other batteries' chemistries.

For this work, a pseudo three-dimensional electrochemical–thermal model was developed for a commercial Type LP2770120 prismatic LiFePO_4 /graphite battery by coupling mass, charge, and energy conservations, as well as electrochemical kinetics. The current collecting tabs of the prismatic battery were also considered. The model treated the battery with current collecting tabs as 3D and the local cell units as 1D. The numerous 1D local electrochemical cell units were connected in parallel by both positive and negative current collectors to constitute the 3D battery. Both electrochemical and thermal characteristics of the battery were studied using this simplified model during the discharge process. A uniformity index characterizing the SOC (state of charge) distributions among 1D cell units was also introduced. This index was used to investigate the effects of the tab placement on the uniformity of the battery cell.

2. Coupled electrochemical–thermal model

2.1. Computational domain and model assumptions

A pseudo three-dimensional electrochemical–thermal model for a single cell in the commercial Type LP2770120 prismatic LiFePO_4 /graphite battery was developed based on the principles of the mass, charge, and energy conservations as well as the electrochemical kinetics. The nominal voltage and capacity of Type LP2770120 are 3.2 V and 16.5 Ah, respectively. Fig. 1 illustrates the computational domain of a pseudo 3D single cell and one of its 1D

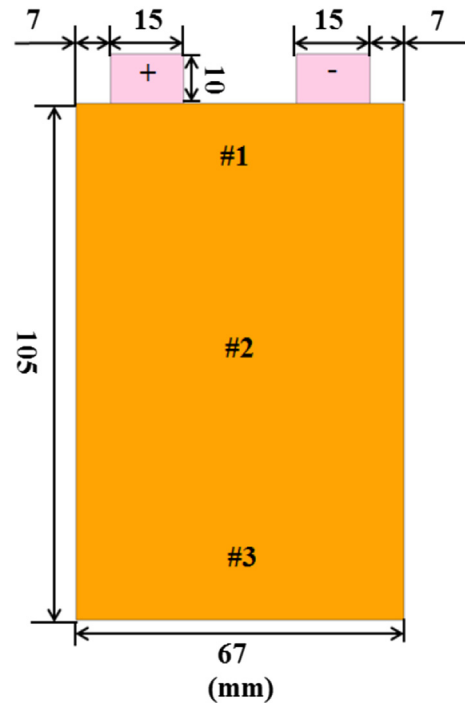


Fig. 2. The dimensions and local regions of the single cell in a prismatic battery.

cell units. Fig. 2 presents the dimensions of the cell. Table 1 lists the application of these conservation equations in each respective domain. The details of these equations will be discussed later in this paper. As shown in Fig. 1, the model treated the single cell with current collectors and tabs as 3D and the local cell units as 1D in the through-plane direction. The local cell unit includes the negative electrode (ne), the separator (sp) and the positive electrode (pe). The current within the local cell unit travels mainly in the through-plane direction (direction z , as shown in Fig. 1) perpendicular to the sandwich structure, and the current parallel to the sandwich structure is negligible. Therefore, we considered each local cell unit as 1D. The 1D local cell units are connected in parallel by current

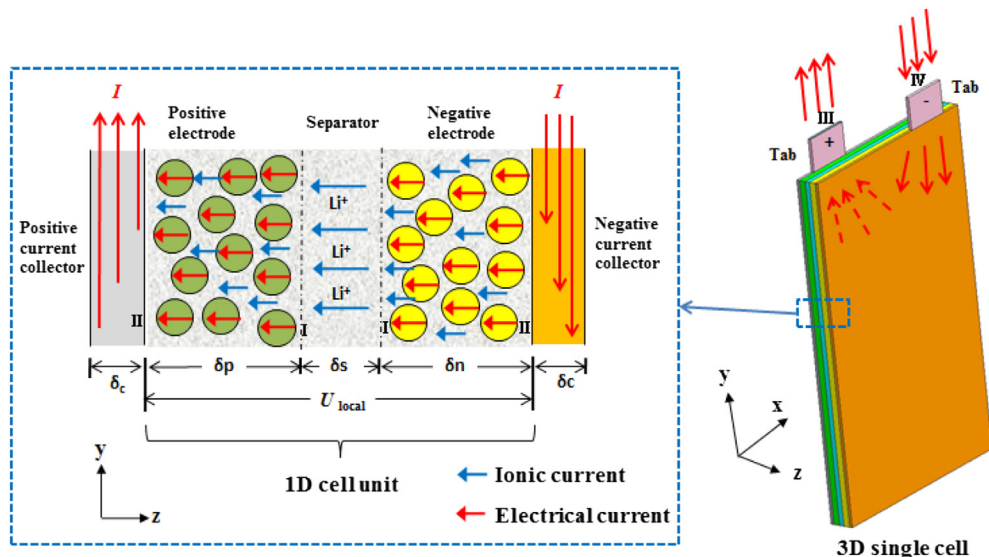


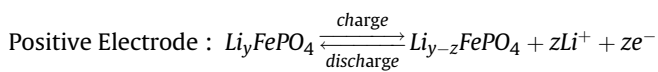
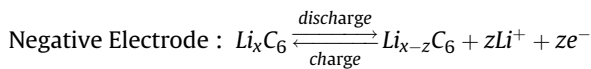
Fig. 1. Schematic graph of the three-dimensional computational domain of a single cell and its one-dimensional cell unit in the prismatic LiFePO_4 battery (during discharge).

Table 1
Governing equations in different computational subdomains.

Governing equations	cc	pe/ne	sp	Tab
Electrochemical kinetics	–	✓	–	–
Charge conservation	✓	✓	✓	✓
Mass conservation	–	✓	✓	–
Energy balance	✓	✓	✓	✓
Reaction heat	–	✓	–	–
Polarization heat	–	✓	–	–
Ohmic heat	✓	✓	✓	✓

collectors of both electrodes to constitute the 3D single cell. The current collectors are responsible for allocating and collecting current for the local cell units. In this model, the electrodes are the porous solid matrix that consists of active particles with spherical shapes of uniform sizes and additives. The positive electrode contains active material particles of iron phosphate (LiFePO_4) and the negative electrode contains the active material particles of graphite (LiC_6). The separator is a porous polymer membrane which constitutes a physical barrier between the two electrodes. Both the electrodes and separator are impregnated with electrolyte, ensuring the transfer of lithium ions between the two electrodes. The electrolyte is a mixture of cyclic and linear carbon solvents in which a lithium salt, lithium hexafluorophosphate LiPF_6 (1.5 mol/L), is dissolved in a nonaqueous 1:1 liquid mixture of EC (ethylene carbonate) and DMC (dimethyl carbonate).

During the discharge process, the electrical current flowing into the negative tab distributes on the negative current collecting plate as shown in Fig 1. The electrical current in the current collector then changes direction and converts to transverse current. The transverse current flows in the through-plane direction of the single cell. The transverse current includes the electrical and ionic currents in both electrode layers, and it equals to only ionic current in the separator layer. The main reason is that both electrolyte and separator do not conduct electrons. Thus, the ionic current in the separator serves as a bridge for the current transfer. The electrochemical reactions that occur at the interface of the electrode and electrolyte during discharge/charge are then:



where x is the stoichiometric coefficient or the number of moles of lithium present in the graphite structure (C_6), y is the stoichiometric coefficient or the number of moles of lithium in the olivine structure of iron phosphate (FePO_4), Li^+ is the lithium ion, and z is the number of moles of lithium taking part in the electrochemical reaction.

2.2. Electrochemical kinetics at the interface

The local charge transfer current density is determined by Butler–Volmer equation in Eq. (1) given below:

$$j_n = j_0 \left\{ \exp\left(\frac{\alpha_a F}{RT} \eta\right) - \exp\left(-\frac{\alpha_c F}{RT} \eta\right) \right\} \quad (1)$$

where j_0 is the exchange current density, α_a and α_c are the anodic and cathodic charge transfer coefficients, η is the local surface

overpotential, and F is the Faraday constant. The exchange current density is calculated by Eq. (2),

$$j_0 = Fk_0 c_2^{\alpha_a} \left(c_{1,\max} - c_{1,\text{surf}} \right)^{\alpha_a} c_{1,\text{surf}}^{\alpha_c} \quad (2)$$

where k_0 is the reaction rate constant, $c_{1,\max}$ is the maximum lithium concentration in the active electrodes and $c_{1,\text{surf}}$ is the lithium concentration on the surface of the active particles. The subscripts 1 and 2 represent the solid phase and electrolyte phase, respectively. The overpotential is defined as

$$\eta = \phi_1 - \phi_2 - U_{eq} \quad (3)$$

where U_{eq} is the open circuit potential of the electrode, ϕ_1 is the solid phase potential, and ϕ_2 is the electrolyte phase potential.

2.3. Charge conservation

The governing equation for charge conservation in the positive/negative electrodes is expressed as

$$\nabla \cdot i_1 + \nabla \cdot i_2 = 0 \quad (4)$$

$$\nabla \cdot i_1 = -S_a j_n \quad (5)$$

$$\nabla \cdot i_2 = S_a j_n \quad (6)$$

where i_1 refers to the electrical current density in the solid phase, i_2 is the ionic current density in the electrolyte phase, and S_a is the specific surface area.

2.3.1. Electron transport in the solid phase

The transport of electrons in the solid phase follows Ohm's law given by Eq. (7),

$$i_1 = -\sigma_1^{\text{eff}} \nabla \phi_1 \quad (7)$$

where σ_1^{eff} refers to the effective electrical conductivity of the solid phase.

2.3.2. Lithium ion transport in electrolyte phase

The transport of lithium ions in the electrolyte is determined by Eq. (8),

$$i_2 = -\sigma_2^{\text{eff}} \nabla \phi_2 + \frac{2RT\sigma_2^{\text{eff}}}{F} \left(1 + \frac{\partial \ln f_{\pm}}{\partial \ln c_2} \right) (1 - t_+) \nabla (\ln c_2) \quad (8)$$

where σ_2^{eff} refers to the effective ionic conductivity of the electrolyte phase, f_{\pm} is the average molar activity coefficient, t_+ is the transferring number of lithium ions in the electrolyte phase, and c_2 is the lithium ion concentration in the electrolyte phase. R is the universal gas constant, and T is the temperature of the electrolyte. As shown in Eq. (8), the ionic current i_2 consists of two terms with the first term following Ohm's law and the second accounting for the ionic concentration gradient.

2.4. Mass conservation

2.4.1. Lithium in active particles

The mass conservation of lithium in the spherical active material particle is described by Eq. (9),

$$\frac{\partial c_1}{\partial t} + \frac{1}{r^2} \frac{\partial}{\partial r} \left(-r^2 D_1 \frac{\partial c_1}{\partial r} \right) = 0 \quad (9)$$

where c_1 is the concentration of lithium in the active material particles of the electrode, t is the time, D_1 represents the diffusion coefficient of lithium in the solid phase, and r is the radial coordinate inside a spherical particle. It is assumed that r cannot exceed the particle's radius (r_0).

2.4.2. Lithium ions in the electrolyte

The mass conservation of lithium ions in the electrolyte is given by Eq. (10),

$$\varepsilon_2 \frac{\partial c_2}{\partial t} + \nabla \cdot J_2 = \frac{S_{aj} n}{F} \quad (10)$$

with

$$J_2 = -D_2^{eff} \nabla c_2 + \frac{i_2 \cdot t_+}{F} \quad (11)$$

where J_2 is the molar flux of lithium ions that consists of two terms: the first term following Fick's law and the second accounting for electromigration, D_2^{eff} represents the effective diffusion coefficient of lithium ions in the electrolyte, and ε_2 is the volume fraction of the electrolyte phase. The term on the right side of the Eq. (10) is zero when applied in the separator.

2.5. Energy balance

The energy balance in the lithium ion battery is given in Eq. (12), in which there are three sources of heat generation: reversible entropic heat q_{rea} , irreversible electrochemical reaction heat q_{act} , and ohmic heat q_{ohm} .

$$\rho c_p \frac{\partial T}{\partial t} - \lambda \nabla^2 T = q_{rea} + q_{act} + q_{ohm} \quad (12)$$

The reversible entropic heat is

$$q_{rea} = S_{aj} n T \frac{\partial U_{eq}}{\partial T} = S_{aj} n T \frac{\Delta S}{F} \quad (13)$$

The irreversible electrochemical reaction heat is

$$q_{act} = S_{aj} n \eta \quad (14)$$

The heat generation due to ohmic losses consists of electrical ohmic heat in the solid phase and ionic ohmic heat in the electrolyte phase

$$q_{ohm} = -i_1 \cdot \nabla \phi_1 - i_2 \cdot \nabla \phi_2 \quad (15)$$

2.6. Temperature and concentration dependent parameters

The positive and negative electrode active materials are $\text{Li}_y\text{-FePO}_4$ and Li_xC_6 , respectively. The electrolyte is 1.5 mol/L LiPF_6 dissolved in a mixture of 1:1 EC/DMC. Table 2 lists battery geometrical and design parameters, kinetic and transport properties, and thermal properties used for modeling.

2.6.1. Electrode kinetics related parameters

In the model, there are two important parameters related to electrode kinetics: reaction rate constant k_0 and OCP (open circuit potential) U_{eq} .

The temperature dependence of reaction rate constant follows the Arrhenius formula [13,20,23,26]

$$k_0(T) = k_{0,ref} \exp \left[\frac{E_{aR}}{R} \left(\frac{1}{T_{ref}} - \frac{1}{T} \right) \right] \quad (16)$$

where E_{aR} is the reaction activation energy, and the constant $k_{0,ref}$ is the reaction rate at the reference temperature T_{ref} .

Table 2
Model parameters for a 16.5 Ah LiFePO_4 battery.

Parameter	Unit	Al foil	Cathode	Separator	Anode	Cu foil	Ref.
ε_1		–	0.435	–	0.56	–	[28]
ε_2		–	0.28	0.4	0.3	–	[35]
δ_i	μm	16	92	20	59	9	[35]
r_0	μm	–	1.15	–	14.75	–	[35]
$c_{2,0}$	mol/m^3	–	–	1500	–	–	[26]
$c_{1,0}$	mol/m^3	–	3900	–	16,361	–	[26]
$c_{1,max}$	mol/m^3	–	26,390	–	31,540	–	[26]
α_a		–	0.5	–	0.5	–	[35]
α_c		–	0.5	–	0.5	–	[35]
$D_{1,ref}$	m^2/s	–	1.25×10^{-15}	–	Eq. (23)	–	[34,35]
D_2	m^2/s	–	–	Eq. (21)	–	–	[29]
E_{aR}	kJ/mol	–	4	–	4	–	[35]
E_{aD}	kJ/mol	–	20	–	4	–	[35]
σ_1	S m^{-1}	3.83×10^7	0.01	–	2	6.33×10^7	[24,34]
σ_2	S m^{-1}	–	–	Eq. (19)	–	–	[29]
k_0	$\text{m}^{2.5} \text{mol}^{-0.5}/\text{s}$	–	3.626×10^{-11}	–	1.764×10^{-11}	–	[26]
t_+		–	–	0.363	–	–	[26]
k_1	$\text{W}/\text{m}\cdot\text{K}$	160	1.48	0.334	1.04	400	[26]
k_2	$\text{W}/\text{m}\cdot\text{K}$	–	–	0.099	–	–	[29]
ρ_1	kg/m^3	2700	1500	492	2660	8900	[29]
ρ_2	kg/m^3	–	–	1210	–	–	[29]
$c_{p,1}$	$\text{J}/\text{kg}\cdot\text{K}$	903	1260.2	1978	1437.4	385	[35]
$c_{p,2}$	$\text{J}/\text{kg}\cdot\text{K}$	–	–	1518	–	–	[29]
T_{ref}	K	–	–	298.15	–	–	[29]
F	C/mol	–	–	96,487	–	–	[35]

The open circuit potential depends on both temperature and concentration of reactants, which can be expressed with a Taylor's series expansion [20]:

$$U_{eq} = U_{eq,ref} + \frac{\partial U_{eq}}{\partial T} (T - T_{ref}) \\ = U_{eq,ref}(SOC, T_{ref}) + \frac{\Delta S(SOC)}{F} (T - T_{ref}) \quad (17)$$

where the SOC (state of charge) of both positive and negative electrodes is determined by Eq. (18).

$$SOC = \frac{c_1}{c_{1,max}} \quad (18)$$

As shown in Eq. (17), both the OCP U_{eq} and the entropy change ΔS depend on the SOC. The dependence of these two variables on the SOC was usually determined by experiments [14,27,28]. Fig. 3 presents how the ΔS and OCP change with the SOC at the reference temperature of 25 °C for Li_yFePO_4 and Li_xC_6 electrodes, respectively.

2.6.2. Electrolyte phase parameters

Equations 19 and 20 describe the temperature and concentration dependence of ionic conductivity σ_2 and thermodynamic factor $(1 + \frac{\partial \ln f_{\pm}}{\partial \ln c_2})(1 - t_+)$ for LiPF_6 in EC/DMC (2:1 by volume) [29–31]:

$$\sigma_2(c_2, T) = 10^{-4} c_2 \times 1.2544 \times \left(-8.2488 + 0.053248T \right. \\ \left. - 0.00002987T^2 + 0.26235 \times 0.001c_2 - 0.0093063 \right. \\ \left. \times 0.001c_2T + 0.000008069 \times 0.001c_2T^2 + 0.22002 \right. \\ \left. \times 10^{-6}c_2^2 - 0.0001765 \times 10^{-6}c_2^2T \right)^2 \quad (19)$$

$$\left(1 + \frac{\partial \ln f_{\pm}}{\partial \ln c_2} \right) (1 - t_+) = \frac{1 - 0.363}{1 - 0.399} \left(0.601 - 0.24 \times 0.01c_2^{0.5} + 0.982 \right. \\ \left. \times [1 - 0.0052(T - 294)](0.001c_2)^{1.5} \right) \quad (20)$$

The Li^+ diffusion coefficient in the electrolyte phase, D_2 , is given in Eq. (21) [29,31–33]:

$$D_2(c_2, T) = 10^{\left(-4.43 - \left(\frac{54}{T - 229 - 5 \times 0.001c_2} \right) - 0.22 \times 0.001c_2 \right) - 4} \quad (21)$$

2.6.3. Solid phase parameters

The temperature dependence of the Li^+ diffusion coefficient D_1 in the solid phase follows the Arrhenius formula [13,20,23,26]

$$D_1(T) = D_{1,ref} \exp \left[\frac{E_{ad}}{R} \left(\frac{1}{T_{ref}} - \frac{1}{T} \right) \right] \quad (22)$$

where E_{ad} is the activation energy for diffusion. In the positive electrode, the constant diffusion coefficient $D_{1,ref}$ at the reference temperature T_{ref} is listed in Table 2, while that in the negative electrode is a function of SOC (state of charge) [34,35]

$$D_{1,ref} = 3.9 \times 10^{-14} (1.5 - SOC)^{3.5} \quad (23)$$

2.7. 1D cell unit parameters

The core of the Li-ion cell unit is treated as 1D sandwich structure. For a 3D battery cell, the balancing of the 1D cell units during discharge will have an effect on the overall performance of the battery. The non-uniformity of the cell units will cause local over-discharge and hot spot, thus reducing the storage capacity and cycle life of the battery. To improve the overall performance of the battery, investigation on the relationship of the transient discharge behaviors between independent 1D cell units as well as the uniformity of the battery is essential.

The working voltage of the local 1D cell unit is the potential difference between its positive and negative current collector:

$$U_{local} = \phi_{cc+} - \phi_{cc-} \quad (24)$$

The open circuit potential of the local 1D cell unit ($U_{eq, local}$) depends on both temperature and average SOC of the electrodes (SOC_{avg}), which can be expressed as:

$$U_{eq,local} = U_{eq,pe} - U_{eq,ne} \quad (25)$$

$$U_{eq,n} = U_{eq,n,ref}(SOC_{avg,n}) + \frac{\partial U_{eq,n}}{\partial T} (T - T_{ref}) \quad (26)$$

The overpotential of the local cell unit can be defined as:

$$\eta_{local} = U_{eq,local} - U_{local} \quad (27)$$

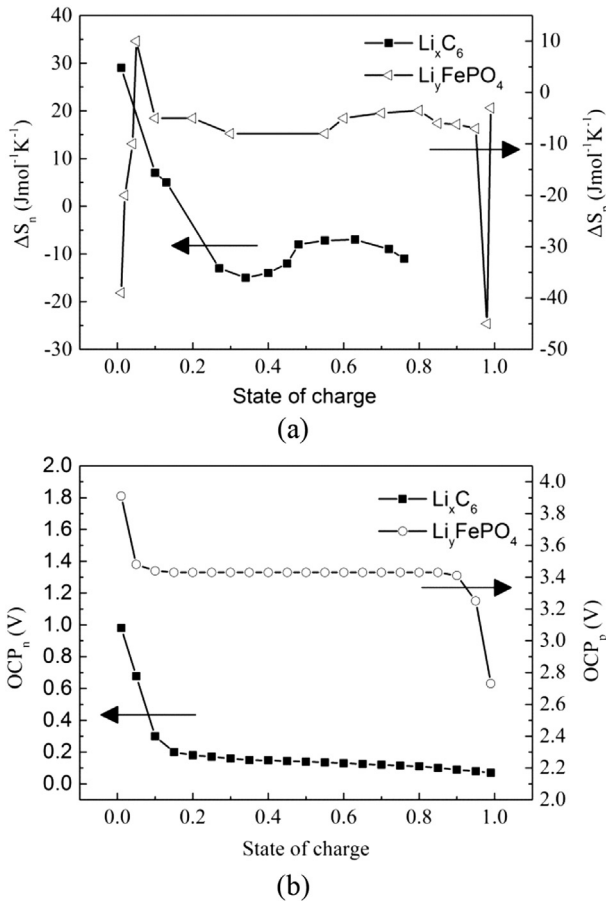


Fig. 3. Thermodynamic properties used in the model as a function of SOC in the electrodes: (a) entropy change [15], (b) reference open circuit potential [16].

2.8. Uniformity index of 1D cell unit SOC

During the discharge process, the working current of 1D cell unit is dependent on its location on the single cell and the discharge time. The average SOC of the cell unit, SOC_{avg} , is determined by its working current density. Thus, the uniformity of the cell unit SOC may reflect the capacity uniformity of the single cell. The uniformity index of cell unit SOC, UI_{SOC} , is defined as:

$$UI_{SOC} = \frac{SOC_{max} - SOC_{min}}{2SOC_{avg}} \quad (28)$$

where SOC_{max} , SOC_{min} , and SOC_{avg} are the maximum, minimum and average values of cell unit SOC, respectively. The lower the value of UI_{SOC} , the better the uniformity of the single cell SOC.

2.9. Boundary and initial conditions

At the electrode/separator interface I as shown in Fig. 1, insulation is specified for the electrical current of the solid phase. Continuity is specified for the ionic current, lithium ion flux of electrolyte phase and heat flux.

$$I: n \cdot i_1 = 0, \quad n \cdot i_2|_{I+} = n \cdot i_2|_{I-}, \quad n \cdot J_2|_{I+} = n \cdot J_2|_{I-}, \quad n \cdot q|_{I+} = n \cdot q|_{I-} \quad (29)$$

At the electrode/current collector interface II, insulation is specified for the ionic current and lithium ion flux of the electrolyte phase. Continuity is specified for the electrical current and heat flux.

$$II: n \cdot i_2 = 0, \quad n \cdot i_1|_{II+} = n \cdot i_1|_{II-}, \quad n \cdot J_2 = 0, \quad n \cdot q|_{II+} = n \cdot q|_{II-} \quad (30)$$

At the positive terminal boundary III, the applied current of the battery is defined as follows

$$III: n \cdot i_1 = i_{app} \quad (31)$$

The negative terminal boundary IV is grounded, thus

$$IV: \phi_1|_{IV} = 0 \quad (32)$$

The working voltage of the battery can be defined as

$$E_{cell} = \phi_1|_{III} - \phi_1|_{IV} \quad (33)$$

At the outer surface, the cell is insulated.

$$-\lambda \frac{\partial T}{\partial n} = 0 \quad (34)$$

The initial conditions of the model are:

$$c_1 = c_{1,0}, \quad c_2 = c_{2,0}, \quad T = T_{ref} \quad (35)$$

3. Numerical simulation and experimental validation

3.1. Numerical simulation

A finite element based commercial software, COMSOL Multiphysics 4.3, was employed to solve the 3D electrochemical–thermal coupled model presented in this paper. A given battery working current density, i_{app} , was applied at the terminal boundary. The

outputs of the model are the battery working voltage, electrical and ionic current density distribution, lithium and li-ion concentration distribution, and temperature field. The MUMPS time dependent solver was chosen with a relative tolerance of 10^{-3} for all the variables; solutions were tested for mesh independence; and the solution time for this model was under 35 min by the computing platform with four quad-core processors (3.2 GHz) and a total of 8 GB RAM (random access memory).

3.2. Experimental validation

A commercial type LP2770120 LiFePO_4 battery (116 mm \times 70 mm \times 27 mm prismatic battery, capacity 16.5 Ah, nominal voltage 3.2 V, 1.5 mol L^{-1} LiPF_6 in EC/DMC solvent) was experimentally tested. A YKLE battery test system was used to monitor the charge–discharge current and voltage. Nine T-type thermocouples were evenly placed on the front surface of the battery. According to the manufacturer, the end-of-discharge voltage for this battery is 2 V. Another stop condition for both charge and discharge is when the total charge/discharge capacity reaches 16.5 Ah. The model validation was conducted by comparing simulation results with experimental data of charging and discharging behaviors at different conditions. The focus will be on thermal validation and electrochemical validation.

3.2.1. Thermal validation

Fig. 4 presents the average temperature on the battery surface obtained by both simulation and experimental measurement. The operating condition for the battery in Fig. 4 was to discharge the battery under different C-rates (0.5C, 1C, 2C) at the initial temperature of 20 °C. The average measured surface temperature is an average of temperatures obtained by the nine thermocouples. As shown in Fig. 4, the average surface temperature increases by around 10 °C, 20 °C, and 35 °C above the ambient temperature for discharge rates of 0.5C, 1C, and 2C, respectively. It also can be seen that the surface temperature increases faster at a higher discharge rate. The variation of temperature profile with discharging time may be due to the internal heat generation, which will be discussed in Section 4.

3.2.2. Electrochemical validation

Fig. 5 shows the battery working voltage during the discharge process under different C-rates (0.5C, 1C, 2C) at the constant

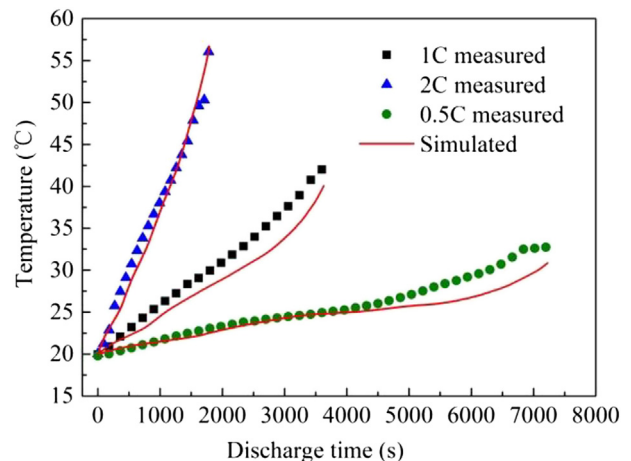


Fig. 4. Comparison of simulated results of average surface temperatures with experimental data during galvanostatic discharge (0.5C, 1C, 2C) under adiabatic condition.

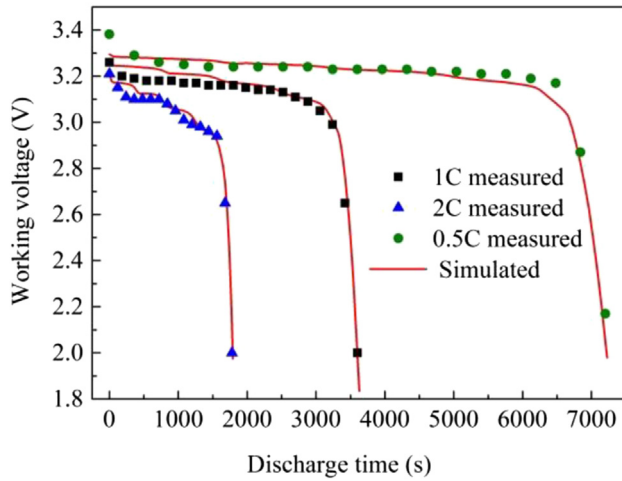


Fig. 5. Comparison of simulated results of working voltage with experimental data during galvanostatic discharge (0.5C, 1C, 2C) under adiabatic condition.

ambient temperature (20 °C). The simulation results agree with the experimental data well, except at the beginning of discharge, where some minor differences between model and experimental data were observed. These differences are related to the thermodynamic data and the design of batteries. For example, the half-cell open circuit potentials for both Li_xFePO_4 and Li_xC_6 electrodes used in this model were not measured values from the experimental battery but instead from published literature; the actual capacity for a new battery is usually larger than that offered by the manufacturer, which has an impact on the initial battery capacity design. If these data were made available for model validation, the remaining discrepancy between the experimental data and simulation results would have been further reduced.

4. Results and discussion

Numerical simulations were performed for the 3D prismatic single cell (as shown in Fig. 1) under 1C, 2C and 5C discharge processes to better understand the electrochemical and thermal characteristics of the prismatic battery. Simulated results of the local 1D cell units are first presented to facilitate analyses and discussion about the heat generation and temperature distribution of the discharge processes.

Fig. 6 shows the distribution of the current density on the negative and positive current collectors during 1C discharge process. The arrows indicate the direction and magnitude of the current flowing in the current collectors. As shown in Fig. 6 (a), all the current flows into the negative current collecting tab from the external circuit and then flows into all the local regions distributed on the entire negative current collector. The magnitude of the current density decreases gradually with increasing distance from the negative tab. In the local regions close to the edge of the current collector, the current density is very small. This is because part of the current flow that arrives at the local regions of the current collector changes its direction to perpendicular to that of the sandwich structure and then flows into the local cell units. This part of the current flowing through the cell unit, as shown in Fig. 7, is called the local working current, i_{local} , which transfers the charges taking part in the electrochemical reaction from the negative electrode to the positive electrode. This can be calculated by Eqs. (7)–(8) with the related boundary conditions (29)–(30). In the battery cell, the current collectors (Cu and Al foil) have a much higher electric conductivity than other functional layers (pe, ne and sp). Thus, the

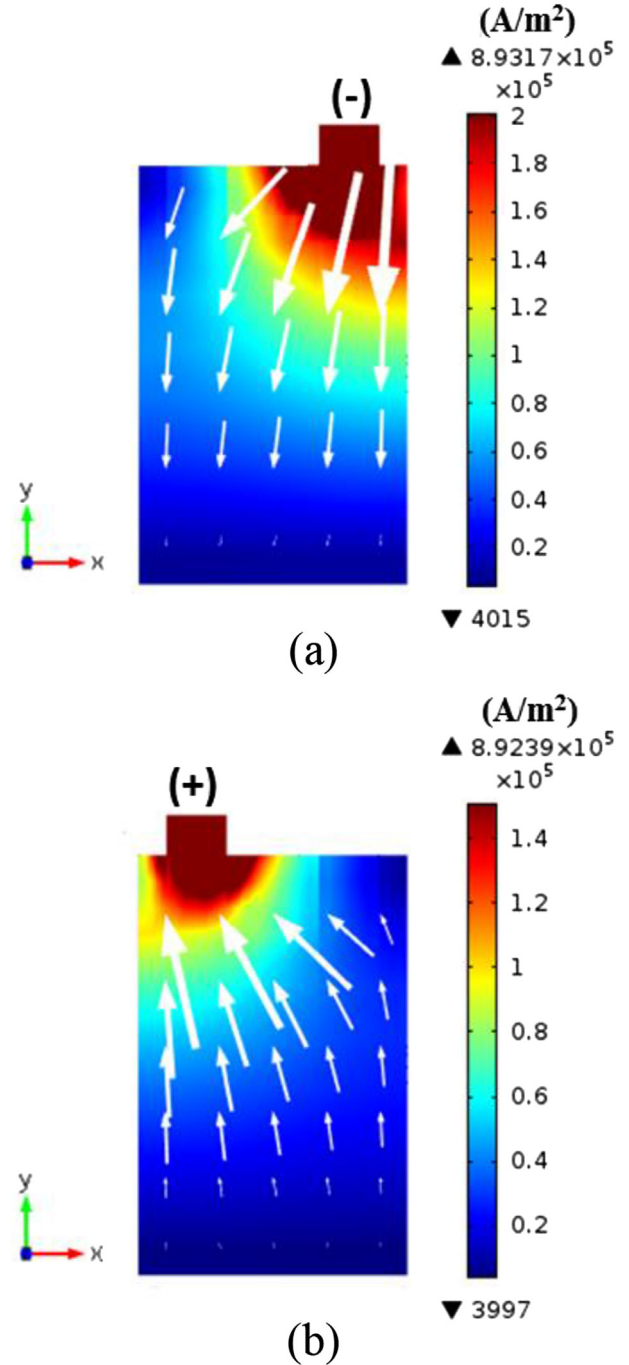


Fig. 6. Current distribution in the (a) negative and (b) positive current collectors during 1C discharge process.

local working current component that is parallel to the sandwich structure within the two electrode layers and the separator is so small that the current flow between the two current collectors can be assumed to be perpendicular to the functional layers (z direction). Therefore, the battery cell can be assumed as a “battery module”, which is composed of many 1D cell units. The current collectors serve as the “wires” connecting the cell units in parallel. The positive and negative tabs serve as the “outlet” and “inlet” of the working current of the single cell, which determine the current direction and potential distribution on the current collectors.

As shown in Fig. 6(b), the positive current collecting tab collects the current flow from all the local cell units to provide it to the

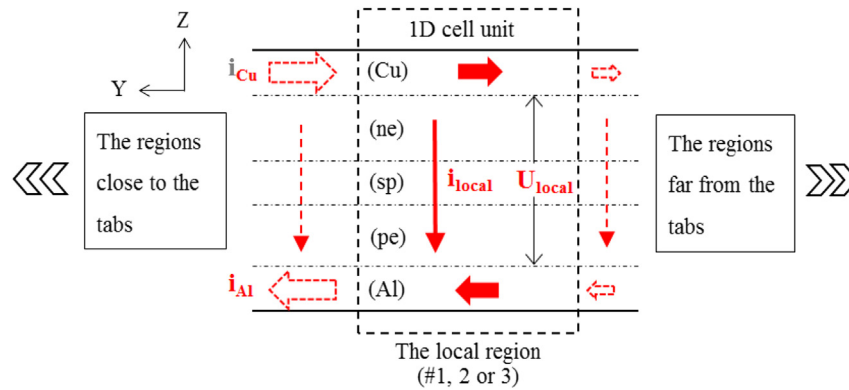


Fig. 7. Schematic diagram of current distribution in a local cell unit.

external circuit. Similar to the current distribution on the negative current collector, the magnitude of the current density on the positive current collector increases gradually with decreasing distance from the positive tab, but the current direction reverses.

The working current flowing through the local 1D cell unit reflects the reaction rate of the local region of the battery cell during discharge process. The working current was determined by the local working voltage (U_{local}), open circuit potential ($U_{eq,local}$), and overpotential (η_{local}). Fig. 8 shows the potential distribution on the positive and negative current collectors during the discharge with 1C rate. It can be seen that the values of the potential of the positive current collector (Fig. 8(a–c)) are around 3.25 V, 3.18 V, and 2.76 V at the discharge time of 3 min, 30 min and 57 min Fig. 8(d) shows the potential distribution on the negative current collector at the discharge time of 3 min, which is also zero since the boundary condition of the negative tab is specially defined as 0 V in the model. According to Ohm's law, the current direction is opposite to that of the potential gradient. This illustrates the relationship between the potential distribution trends shown in Fig. 8 and the current direction in Fig. 6. The positive and negative current collecting tabs are placed on the same side of this kind of prismatic battery. However, as shown in Fig. 6, the current direction is from the tab to the entire region on the negative current collector but reverses on the positive current collector. This leads to completely different potential variation trends on the positive and negative current collectors, as shown in Fig. 8.

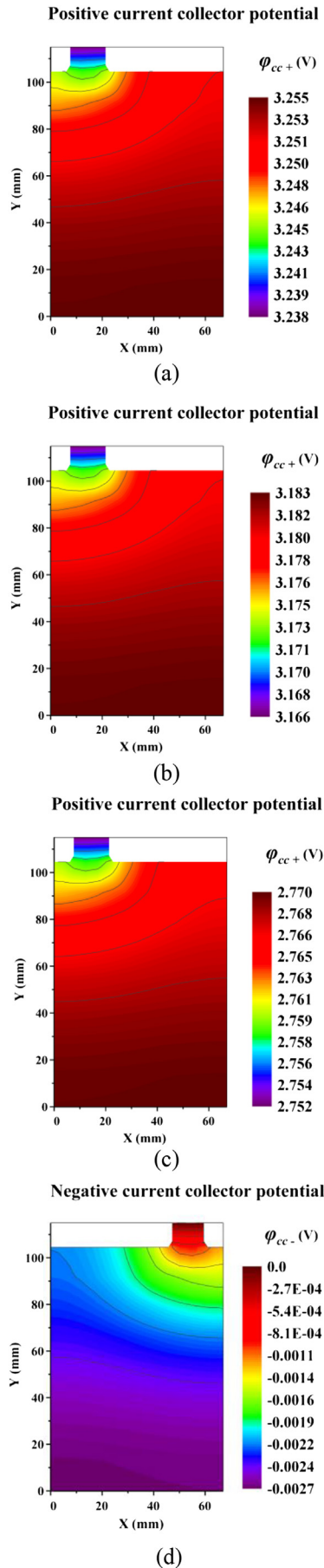
Fig. 9 shows that the distribution of the cell unit working voltage is uneven within the entire battery during the 1C discharge process. By 50% SOC (30 min), the potential of the positive current collector drops slightly, which complies with the stable discharge voltage platform of LiFePO_4 battery. A large potential gradient exists in the region close to the positive tab, because the positive current collector Al foil has lower conductivity than the negative current collector Cu foil. The uneven local working voltage reflects the non-uniformity of the reaction rate of the battery cell to some extent.

The local overpotential is the driving force for the electrochemical reaction. Fig. 10 shows the local open circuit potential ($U_{eq,local}$) and the local working voltage (U_{local}) of the #1 cell unit during 1C discharge process. Overall, the local OCP decreases with discharge time. Near the end of the discharge process, the local cell unit OCP changes rapidly because of the high sensitivity of the OCP on the SOC of the cell unit. The local working voltage is determined by the potential of both positive and negative current collectors, which are sensitive to the location of the cell unit, as shown in Fig. 9. Thus, as for the local cell unit, the overpotential mainly relates to the average SOC of the 1D cell unit and its location in the battery cell.

Fig. 11 shows the comparison of overpotentials for three different local cell units during 1C discharge process. The cell unit #1, which is close to the tabs, has the maximum overpotential during the early and middle period of discharge; towards the end of discharge, the maximum overpotential shifts from the cell unit #1 to #3 which is far from the tabs. Generally, a greater overpotential would drive the electrochemical reaction of the electrode at a faster rate, which can be directly measured by the working current density of the local cell unit.

Fig. 12 shows the distribution of the local working current density of a single cell during discharge at 1C rate. At the beginning of discharge (Fig. 12(a)), the cell unit working current density increases from the region distant from the tabs to that close to the tabs (in the y coordinate). During the middle period of discharge (Fig. 12(b)), the working current density becomes more uniform. At the end of discharge (Fig. 12(c)), the working current density decreases in the y coordinate, which is completely opposite to the distribution trend in the early discharge period. During the entire discharge process, the maximum local working current density location shifts from the tabs side to the other side of the single battery cell, indicating the electrochemical reaction rate of the cell units is not in a uniform mode throughout the discharge process. Especially for the region close to the positive tab, it has the fastest reaction rate at the beginning but slowest by the end of discharge.

Fig. 13 shows the working current density of three local cell units under 1C, 2C and 5C discharge. Under 1C rate (Fig. 13(a)), the average working current of the three cell units is approximately 19 A/m^2 , which keeps constant all through the discharge due to the constant current discharge of the single cell. Inspection of the temporal variation curves of #1, #2 and #3 reveals that the #1 unit has a generally opposite variation tendency to the #3 curve although they all fluctuate during discharge. The working current of cell unit #1 is greatest at the beginning and decreases with wave all through the discharge, while the #3 has the minimum value at the beginning and increases with wave by the end of discharge. The three variation curves are consistent with the observations from Fig. 12. Fig. 13 also shows that all the three curves have a similar relationship during discharge to the cell unit overpotential curves as shown in Fig. 11. Therefore, the cell unit working current is driven by its overpotential, which is determined by local cell unit OCP and working voltage as shown in Fig. 10. Moreover, in the 1D cell unit model, the local cell unit OCP (Eq. (25)) and working voltage (Eq. (24)) are calculated by OCP-SOC curve (Fig. 3) and Butler–Volmer equation (Eq. (1)). The average SOC of the cell unit decreases during the discharge, which may determine the local OCP of the cell unit. The cell unit with a greater working current density (reaction rate) may be in a more utilized state which means a smaller average SOC.



The local cell unit working voltage is obtained from the potential distribution, which is determined by the location of the cell unit, as shown in Fig. 9. During 2C and 5C discharge process (Fig. 13(b, c)), the local variation curves have the similar distribution trend to that of 1C discharge process. The average working current density (38 A/m² for 2C and 95 A/m² for 5C) increases proportionally with the discharge rate of the single cell.

The heat sources during the charge–discharge processes of LiFePO₄/graphite battery include the reaction heat, the irreversible electrochemical reaction heat, and the ohmic heat. Fig. 14 plots the total heat generation rates of the local cell units under different discharge rates. During 1C discharge (Fig. 14(a)), the total heat generation of all the three local cell units decreases a little at the beginning of discharge (before 400 s), and then remains almost unchanged in the middle period. The total heat generation increases in the late period (after 2500 s) of the discharge process. During 2C discharge process (Fig. 14(b)), the heat generation decreases first (before 250 s) and then increases with wave until the end of the discharge process. During 5C discharge process (Fig. 14(c)), the overall heat generation increases all through the discharge process. At any instant during the initial and middle period of discharge at all discharge rates, the 1# cell unit has the maximum heat generation while the 3# cell unit has the minimum heat generation. However, toward the end of discharge, the heat generation of 3# cell unit becomes more dominant, but the 1# cell is at a minimum. The three groups of heat generation rate variation curves (Fig. 14(a–c)) are in accordance to the observations from Fig. 13. This is because the discharge process of the cell unit is an exothermic process. The local cell unit with a greater working current density has higher heat generation rate during discharge process. In addition, the total heat generation rate is approximate 10, 40 and 200 kW/m³ for 1C, 2C and 5C, which increases approximately with the square of the discharge rate of the single cell.

Fig. 15 shows the temperature distribution of the single cell under various discharge rates. The maximum temperature difference, between the hottest and the coldest spots, during 1C, 2C and 5C discharge are 0.3 K, 1 K, and 7.2 K, respectively. The temperature is higher in the region close to the tabs than that distant from the tabs. The reason is that, as shown in Fig. 14, the heat generation is much faster in the tab side during most of the discharge process. In addition, the temperature decreases with increase of x , from the positive to the negative tab. This phenomenon can be further explained by the results shown in Fig. 16. As indicated by Fig. 16, the heat generation of the positive current collector is the predominant heat source in the region close to the tabs (#1 cell unit) during 1C, 2C and 5C discharge process. However, as shown in Fig. 6(b), on the positive current collector close to the tabs, the current density in the positive tab side is greater than that in the negative tab side. Thus, higher ohmic heat in the positive current collector may be generated in the region close to the positive tab.

The difference between the 1D cell unit model and the 3D single cell model developed in this paper is that the 3D model has the positive and negative tabs attached to the current collectors. The placement of tabs can affect the current distribution on the current collectors, which generate potential gradient on both current collectors. To investigate the effect of the tab location and the discharge rate on the uniformity of the battery, another prismatic single cell model was developed. This cell, named as type B shown in Fig 17, was used to compare with the single cell, type A, discussed

Fig. 8. Potential distributions on the positive current collector (a, b, c) and the negative current collector (d) during discharge with 1C rate. Discharge time is: (a, d) 3 min, (b) 30 min, and (c) 57 min.

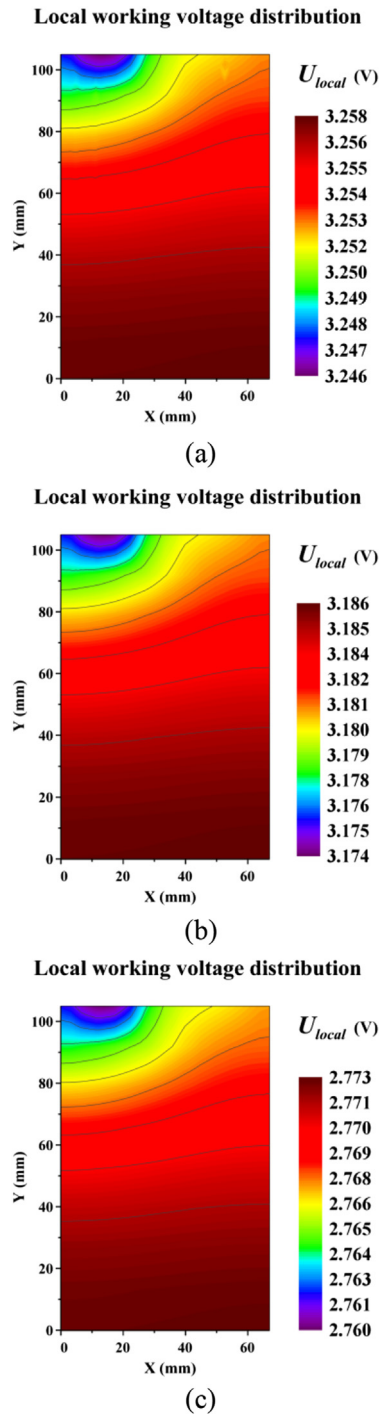


Fig. 9. Distribution of the cell unit working voltage. Discharge time is: (a) 3 min, (b) 30 min, and (c) 57 min.

previously in this paper. The only difference between two cells is that the negative tab of type B is placed on the opposite side of that of type A. The design parameters of type A and type B single cells are same except the location of the tabs.

The uniformity index of cell unit SOC was defined in Eq. (28) to present the uniformity of current density distribution. The lower the uniformity index, more uniform the cell current. Fig. 18 shows uniformity index of cell unit SOC vs. average DOD (depth of discharge) for type A and type B cells during 1C, 2C and 5C discharge process. For each type of single cell, the value of U_{SOC} is higher at a high

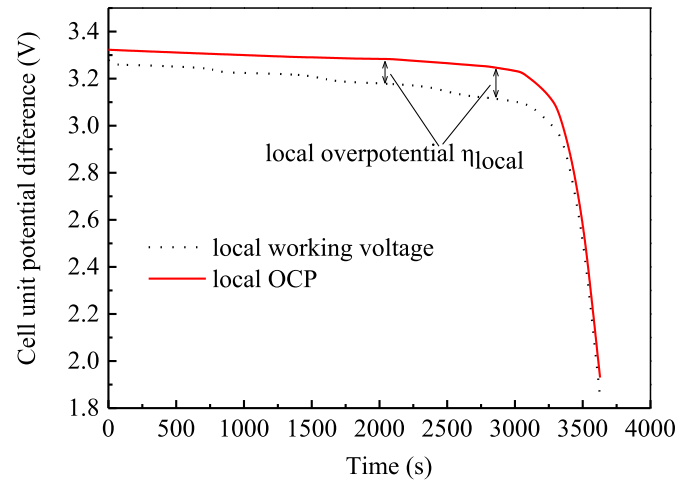


Fig. 10. #1 cell unit potential difference vs. time plots during 1C discharge process.

discharge rate than at a low discharge rate. Therefore the uniformity of the battery becomes better at a lower discharge rate. In the low rate of 1C and 2C discharge for both type A and B cells, the U_{SOC} increases during the initial and middle long period (DOD < 0.85), but it decreases sharply by the end (DOD > 0.85) of discharge. However, at the high rate of 5C discharge for both type A and B, the U_{SOC} increases throughout the discharge process. This trend illustrates that the non-uniformity of the battery becomes more pronounced as the DOD increases throughout the high rate (5C) discharge as well as before the late period of low rate (1C and 2C) discharge. However the non-uniformity disappears quickly during the late period of low rate (1C and 2C) discharge. This phenomenon agrees with the observations from Fig. 13. The local working current density of the three local cell units tends to become uniform quickly towards the end of discharge at low rate, but not at high discharge rate. At the same discharge rates, the U_{SOC} of the type B cell is lower than that of the type A throughout the discharge process. The type B cell is favorable to the uniform utilization of the cell units. It can be deduced that the location of the current collecting tabs has an effect on the uniformity of the battery. In terms of the working mechanism of the battery cell with tabs analyzed above, the type B cell has an optimized potential and current distribution for improving the uniformity of the battery as compared to the type A cell.

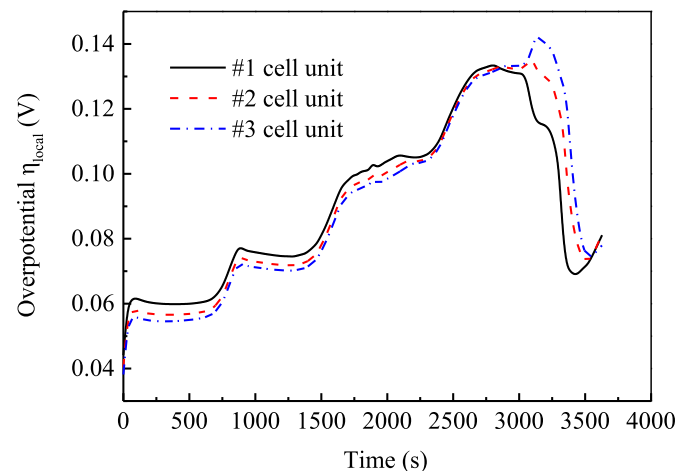


Fig. 11. Cell unit overpotential of different local cell units during 1C discharge processes.

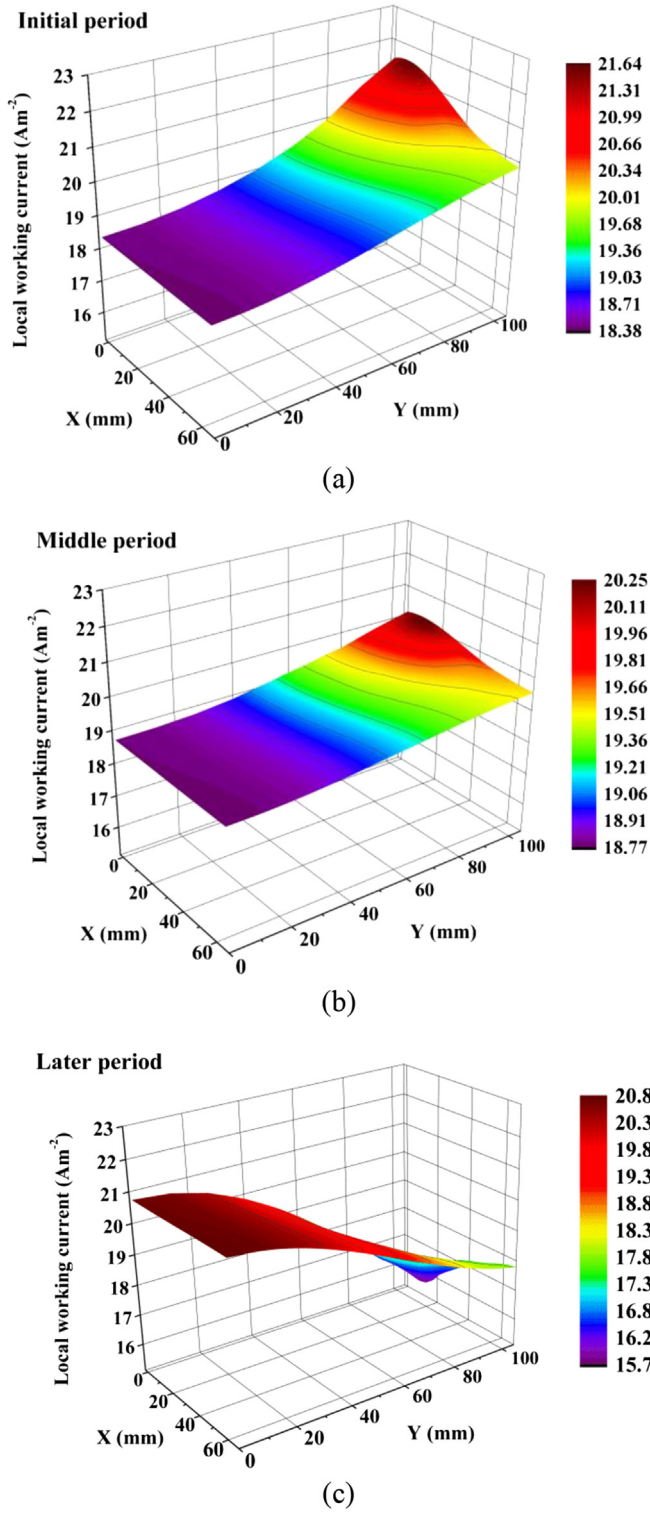


Fig. 12. Distributions of the local working current density (absolute value) of the single cell during discharge at 1C rate. Discharge time is: (a) 3 min, (b) 30 min, and (c) 57 min.

5. Conclusion

A pseudo 3D electrochemical–thermal coupled model has been developed for a commercial Type 38120 LiFePO₄ prismatic power battery. The current collecting tabs on the battery have been taken into consideration. The modeling results are further validated for

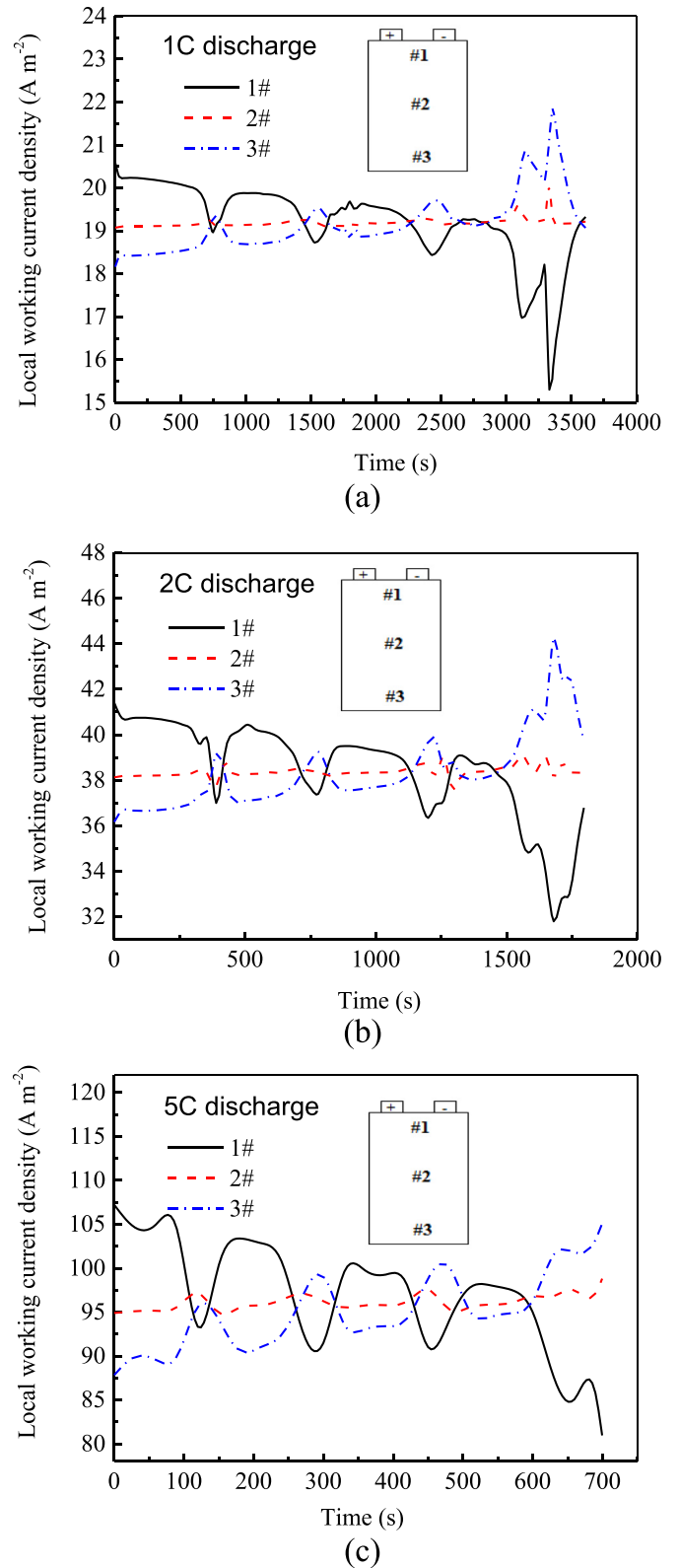


Fig. 13. The working current density vs time plots of the different local cell units under 1C (a), 2C (b) and 5C (c) discharge processes.

both electrochemical performances and thermal behavior using experimental data. The model treated the battery with many 1D local cell units connected in parallel by 3D current collecting tabs. The model presented the non-uniform distribution of the working

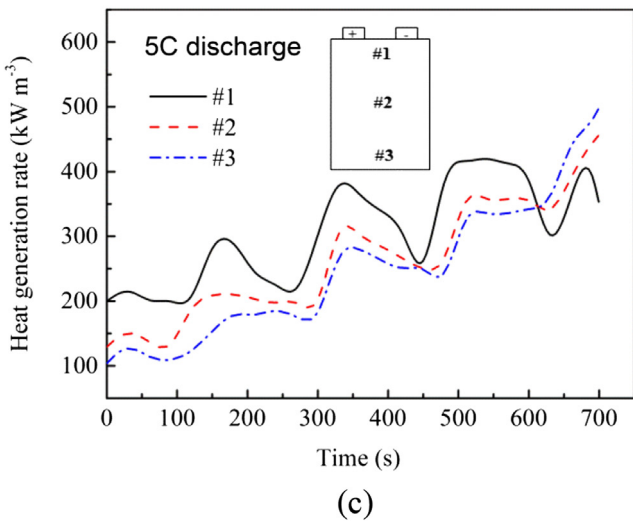
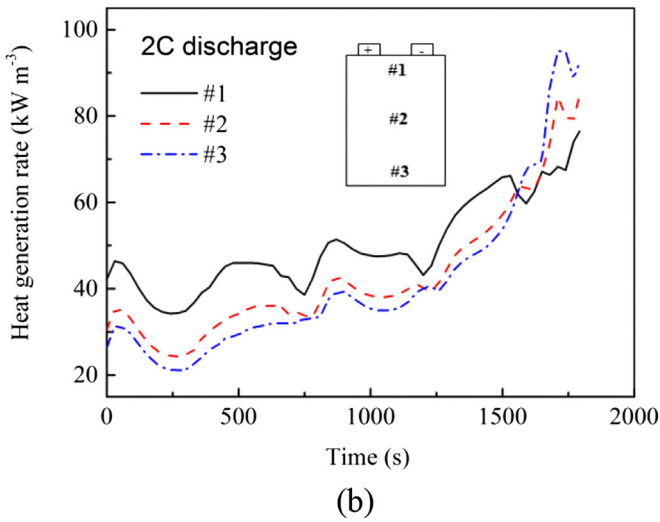
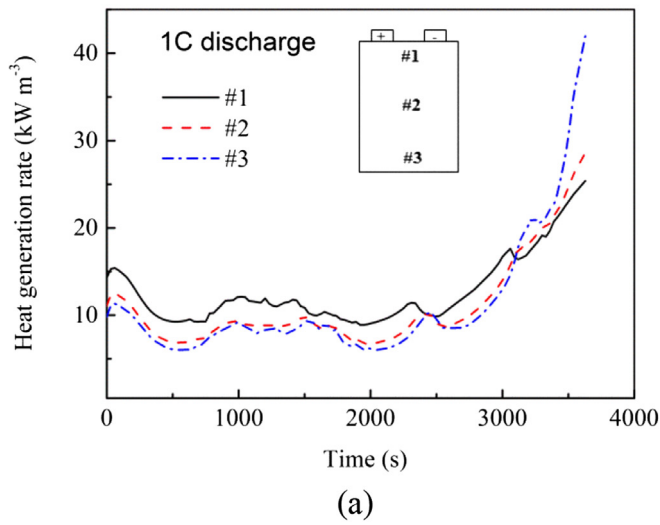


Fig. 14. Total heat generation rates of the local cell units under 1C (a), 2C (b) and 5C (c) discharge rates.

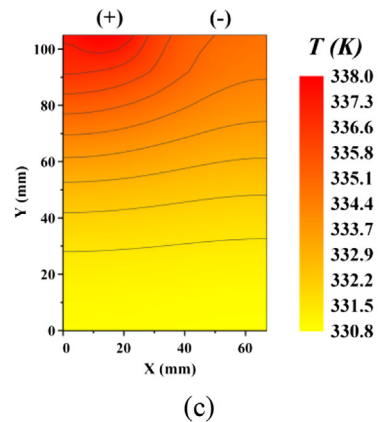
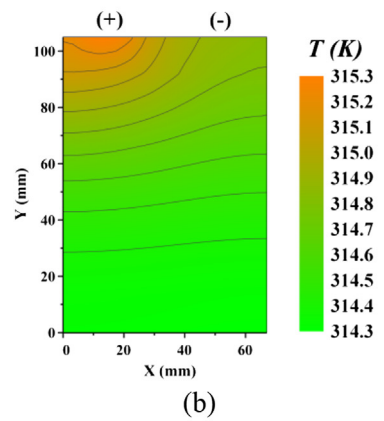
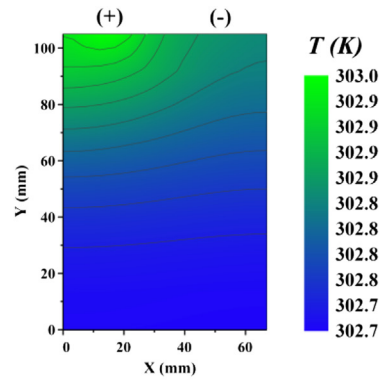


Fig. 15. Temperature distribution during (a) 1C, (b) 2C and (c) 5C discharge process. Discharge time is: (a) 1020 s, (b) 990 s, and (c) 360 s.

voltage, overpotential, electrochemical reaction rate and heat generation rate of the cell during discharge process.

It is concluded that:

- The overpotential of the local 1D cell unit is determined by its working voltage and open circuit potential, and it is the driving force of the local electrochemical reaction.
- During the discharge process, the distribution of the reaction rate of the local cell units is not in a uniform mode due to the electrical gradient on the current collectors.
- The higher reaction rate the local cell unit has, the more quickly the heat is generated in the local region. The heat generation rate among the different regions is not uniform due to the non-uniform distributed reaction during the entire discharge cycle.

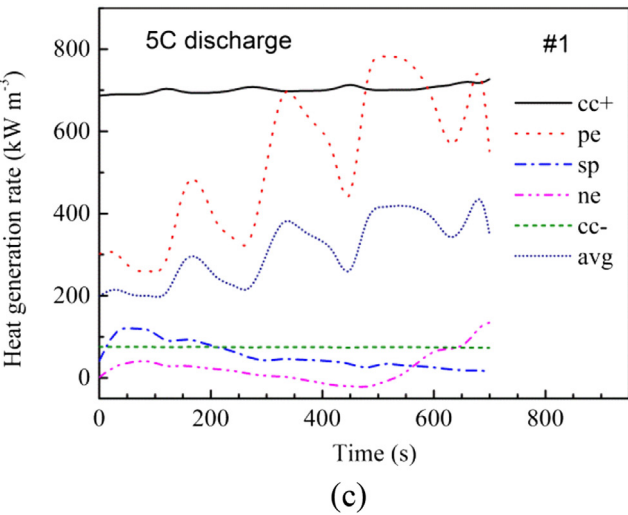
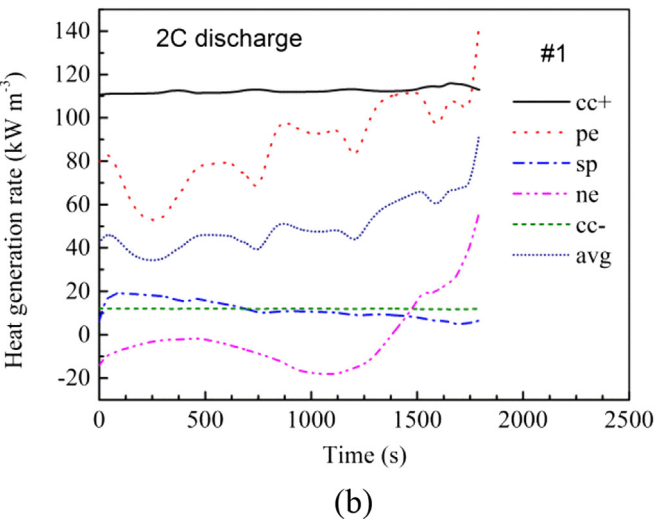
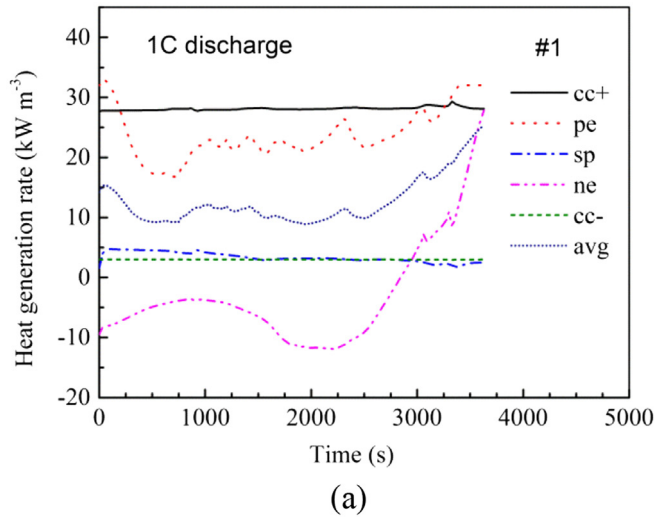


Fig. 16. Heat generation in the various function layers of the #1 cell unit under (a) 1C, (b) 2C and (c) 5C discharge rates.

- The temperature is higher in the region close to the tabs than that distant from the tabs, because the heat generation is much faster in the tab side during most of the discharge process.

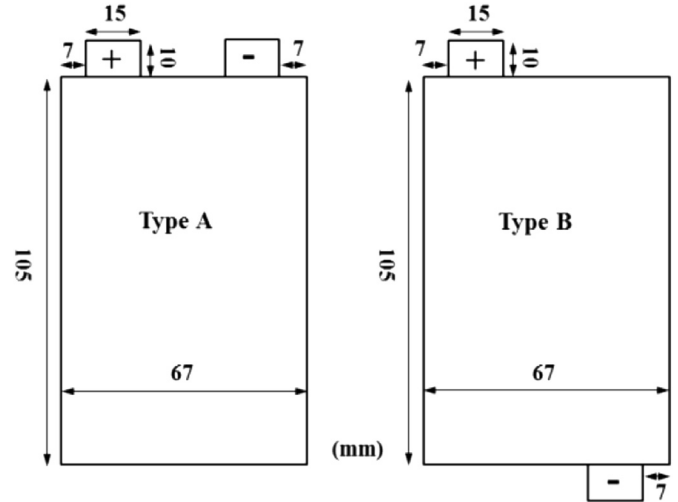


Fig. 17. Schematic diagrams of the tabs location for type A and type B single cell.

- The placement of the positive and the negative current collecting tabs has a significant effect on the distributions of its potential and local reaction rates, which therefore affects the heat generation rates, and thus the temperature distribution within the battery.
- Battery cells with tabs placed on opposite sides have more uniform electrical and thermal distribution than those with tabs on the same side.

The model can be extended to include the effect of the electrical contact resistance between the terminals and the tabs of the cell, geometrical dimensions of the current collecting tabs and the heat dissipation on the battery surface.

The methodology of developing battery discharging model presented in this work can be applied to model the charging process as well. However, many model parameters should be modified for the application in charging process. For example, depending on cell specifications, charging conditions are usually different from discharging conditions. Therefore, the boundary conditions of the model must be changed accordingly to be applied for charging process. Additionally, the reaction constant should be different

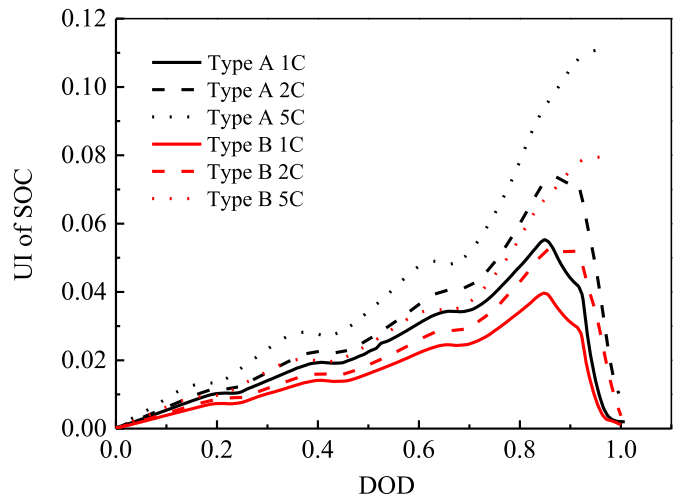


Fig. 18. UI of SOC vs. average DOD for type A and type B single cells during 1C, 2C and 5C discharge process.

between charging and discharging process as well as heat sources. The battery during charging usually exhibits higher heat generation than discharging due to high internal resistance. Future research will explore heat generation of batteries during charging process, and the results will be compared to heat generating in discharging process.

Acknowledgments

The authors would like to thank for support of this work by the National Natural Science Foundation of China (No. 51376018) and Beijing Natural Science Foundation (3142014).

Nomenclature

c_1	concentration of lithium in the active material particles (mol m^{-3})
c_2	electrolyte concentration (mol m^{-3})
$c_{1,\text{max}}$	maximum concentration of lithium in the active material (mol m^{-3})
$c_{1,\text{surf}}$	surface concentration of lithium in the active material (mol m^{-3})
D_1	diffusion coefficient of lithium in the active material ($\text{m}^2 \text{s}^{-1}$)
D_2	diffusion coefficient of electrolyte ($\text{m}^2 \text{s}^{-1}$)
E_{aD}	diffusion activation energy (kJ (mol)^{-1})
E_{aR}	reaction activation energy (kJ (mol)^{-1})
E_{cell}	working voltage of the battery (V)
f_{\pm}	average molar activity coefficient
F	Faraday's constant (C mol^{-1})
h	lumped heat transfer coefficient ($\text{W m}^{-2} \text{K}^{-1}$)
i_0	local working current density of the cell unit (A m^{-2})
i_{app}	applied working current density of the battery (A m^{-2})
j_0	exchange current density (A m^{-2})
j_n	local charge transfer current density (A m^{-2})
k_0	reaction rate constant ($\text{m}^{2.5} \text{mol}^{-0.5} \text{s}^{-1}$)
k	thermal conductivity (W (mK)^{-1})
q	volumetric heat generation (W m^{-3})
q_{rea}	reversible entropy heat generation (W m^{-3})
q_{act}	irreversible electrochemical reaction heat generation (W m^{-3})
q_{ohm}	ohmic heat generation (W m^{-3})
R	gas constant, $8.314 \text{ (J mol}^{-2} \text{K}^{-1})$
r	radius distance variable of electrode particles (μm)
r_0	radius of electrode particles (μm)
S_a	specific surface area (m^{-1})
SOC	state of charge
t	time (s)
t_+	transferring number of Li^+
T	cell temperature (K)
T_{amb}	ambient temperature (K)
U_{eq}	open circuit potential of the electrode (V)
U_{ref}	open circuit potential under the reference temperature (V)

Greek letters

α_a	anodic transfer coefficient
α_c	cathodic transfer coefficient
ε_1	active material volume fraction
ε_2	electrolyte volume fraction
ϕ_1	solid phase potential (V)
ϕ_2	electrolyte phase potential (V)
γ	Bruggeman tortuosity exponent
σ_1	electronic conductivity of solid matrix (S m^{-1})
σ_2	ionic conductivity of electrolyte (S m^{-1})

δ_i	thickness of each battery component (μm)
η	local surface overpotential (V)

Subscripts, superscripts and acronyms

0	initial or equilibrated value
1	solid phase
2	electrolyte phase
<i>amb</i>	ambient
<i>cc</i>	current collector
<i>eff</i>	effective value
<i>el</i>	electrolyte
<i>ne</i>	current collector
<i>pe</i>	positive electrode
<i>ref</i>	reference value
<i>sp</i>	separator
<i>surf</i>	surface of active material particles
term+/-	positive/negative terminal

References

- [1] Kang J, Yan F, Zhang P, Du C. Comparison of comprehensive properties of Ni-MH (nickel-metal hydride) and Li-ion (lithium-ion) batteries in terms of energy efficiency. *Energy* 2014;70:618–25.
- [2] Krieger EM, Cannarella J, Arnold CB. A comparison of lead-acid and lithium-based battery behavior and capacity fade in off-grid renewable charging applications. *Energy* 2013;60:492–500.
- [3] Hu X, Li SE, Jia Z, Egardt B. Enhanced sample entropy-based health management of Li-ion battery for electrified vehicles. *Energy* 2014;64:953–60.
- [4] Fathabadi H. High thermal performance lithium-ion battery pack including hybrid active-passive thermal management system for using in hybrid/electric vehicles. *Energy* 2014;70:529–38.
- [5] Zhang XW, Kong X, Li G, Li J. Thermodynamic assessment of active cooling/heating methods for lithium-ion batteries of electric vehicles in extreme conditions. *Energy* 2014;64:1092–101.
- [6] Guo M, White RE. A distributed thermal model for a Li-ion electrode plate pair. *J Power Sources* 2013;221:334–44.
- [7] Rahn CD, Wang CY. *Battery systems engineering*. John Wiley & Sons; 2012.
- [8] Hu X, Li S, Peng H. A comparative study of equivalent circuit models for Li-ion batteries. *J Power Sources* 2012;198:359–67.
- [9] Saw LH, Ye Y, Tay AAO. Electro-thermal characterization of Lithium Iron Phosphate cell with equivalent circuit modeling. *Energy Convers Manage* 2014;87:367–77.
- [10] Patil RS, Juvekar VA. Analysis of multiparticle bipolar electrolysis using single particle cell model. *Chem Eng Sci* 2014;110:72–82.
- [11] Safari M, Delacourt C. Mathematical modeling of lithium iron phosphate electrode: galvanostatic charge/discharge and path dependence. *J Electrochem Soc* 2011;158:A63–73.
- [12] Doyle M, Fuller TF, Newman J. Modeling of galvanostatic charge and discharge of the lithium/polymer/insertion cell. *J Electrochem Soc* 1993;140:1526–33.
- [13] Bernardi D, Pawlikowski E, Newman J. A general energy balance for battery systems. *J Electrochem Soc* 1985;132:5–12.
- [14] Arora P, Doyle M, White RE. Mathematical modeling of the lithium deposition overcharge reaction in lithium-ion batteries using carbon-based negative electrodes. *J Electrochem Soc* 1999;146:3543–53.
- [15] Pals CR, Newman J. Thermal modeling of the lithium/polymer battery I. Discharge behavior of a single cell. *J Electrochem Soc* 1995;142:3274–81.
- [16] Pals CR, Newman J. Thermal modeling of the lithium/polymer battery II. Temperature profiles in a cell stack. *J Electrochem Soc* 1995;142:3282–8.
- [17] Bandhauer TM, Garimella S, Fuller TF. A critical review of thermal issues in lithium-ion batteries. *J Electrochem Soc* 2011;158:R1–25.
- [18] Ramadesigan V, Northrop PW, De S, Santhanagopalan S, Braatz RD, Subramanian VR. Modeling and simulation of lithium-ion batteries from a systems engineering perspective. *J Electrochem Soc* 2012;159:R31–45.
- [19] Forgez C, Vinh Do D, Friedrich G, Morcrette M, Delacourt C. Thermal modeling of a cylindrical LiFePO_4 /graphite lithium-ion battery. *J Power Sources* 2010;195:2961–8.
- [20] Guo M, Sikha G, White RE. Single-particle model for a lithium-ion cell: thermal behavior. *J Electrochem Soc* 2011;158:A122–32.
- [21] Somasundaram K, Birgersson E, Mujumdar AS. Thermal-electrochemical model for passive thermal management of a spiral-wound lithium-ion battery. *J Power Sources* 2012;203:84–96.
- [22] Gu WB, Wang CY. Thermal-electrochemical modeling of battery systems. *J Electrochem Soc* 2000;147:2910–22.
- [23] Hellwig C, Sörgel S, Bessler WG. A multi-scale electrochemical and Thermal model of a LiFePO_4 battery. *Ecs Trans* 2011;35:215–28.
- [24] Srinivasan V, Newman J. Discharge model for the lithium iron-phosphate electrode. *J Electrochem Soc* 2004;151:A1517–29.

- [25] Thorat IV, Joshi T, Zaghbi K, Harb JN, Wheeler DR. Understanding rate-limiting mechanisms in LiFePO₄ cathodes for Li-ion batteries. *J Electrochem Soc* 2011;158:A1185–93.
- [26] Ye Y, Shi Y, Cai N, Lee J, He X. Electro-thermal modeling and experimental validation for lithium ion battery. *J Power Sources* 2012;199:227–38.
- [27] Viswanathan VV, Choi D, Wang D, Xu W, Towne S, Williford RE, et al. Effect of entropy change of lithium intercalation in cathodes and anodes on Li-ion battery thermal management. *J Power Sources* 2010;195:3720–9.
- [28] Safari M, Delacourt C. Modeling of a commercial graphite/LiFePO₄ cell. *J Electrochem Soc* 2011;158:A562–71.
- [29] Doyle M, Newman J, Gozdz AS, Schmutz CN, Tarascon JM. Comparison of modeling predictions with experimental data from plastic lithium ion cells. *J Electrochem Soc* 1996;143:1890–903.
- [30] Valøen LO, Reimers JN. Transport properties of LiPF₆-based Li-ion battery electrolytes. *J Electrochem Soc* 2005;152:A882–91.
- [31] Capiglia C, Saito Y, Kageyama H, Mustarelli P, Iwamoto T, Tabuchi T, et al. 7Li and 19F diffusion coefficients and thermal properties of non-aqueous electrolyte solutions for rechargeable lithium batteries. *J Power Sources* 1999;81:859–62.
- [32] Capiglia C, Saito Y, Yamamoto H, Kageyama H, Mustarelli P. Transport properties and microstructure of gel polymer electrolytes. *Electrochim Acta* 2000;45:1341–5.
- [33] Fang W, Kwon OJ, Wang CY. Electrochemical–thermal modeling of automotive Li-ion batteries and experimental validation using a three-electrode cell. *Int J Energy Res* 2010;34:107–15.
- [34] Wu W, Xiao X, Huang X. The effect of battery design parameters on heat generation and utilization in a Li-ion cell. *Electrochim Acta* 2012;83:227–40.
- [35] Jiang F, Peng P, Sun Y. Thermal analyses of LiFePO₄/graphite battery discharge processes. *J Power Sources* 2013;243:181–94.